The Astrophysical Journal, 827:108 (15pp), 2016 August 20 doi:10.3847/0004-637X/827/2/108

MEASUREMENTS OF EXTRAGALACTIC BACKGROUND LIGHT FROM THE FAR UV TO THE FAR IR FROM DEEP GROUND- AND SPACE-BASED GALAXY COUNTS

Simon P. Driver[1,5], Stephen K. Andrews[1], Luke J. Davies[1], Aaron S. G. Robotham[1], Angus H. Wright[1], Rogier A. Windhorst[2], Seth Cohen[2], Kim Emig[2], Rolf A. Jansen[2], and Loretta Dunne[3,4]
[1] International Centre for Radio Astronomy Research (ICRAR), The University of Western Australia, M468, 35 Stirling Highway, Crawley, WA 6009, Australia; simon.driver@uwa.edu.au
[2] School of Earth & Space Exploration, Arizona State University, Tempe, AZ 85287-1404, USA
[3] School of Physics and Astronomy, Cardiff University, Queen's Buildings, Cardiff CF24 3AA, UK
[4] Institute for Astronomy, Royal Observatory, Blackford Hill, Edinburgh EH9 3HJ, UK
Received 2016 February 26; revised 2016 May 2; accepted 2016 May 4; published 2016 August 12

ABSTRACT

We combine wide and deep galaxy number-count data from the Galaxy And Mass Assembly, COSMOS/G10, *Hubble Space Telescope* (*HST*) Early Release Science, *HST* UVUDF, and various near-, mid-, and far-IR data sets from ESO, *Spitzer*, and *Herschel*. The combined data range from the far UV (0.15 μm) to far-IR (500 μm), and in all cases the contribution to the integrated galaxy light (IGL) of successively fainter galaxies converges. Using a simple spline fit, we derive the IGL and the extrapolated IGL in all bands. We argue that undetected low-surface-brightness galaxies and intracluster/group light are modest, and that our extrapolated-IGL measurements are an accurate representation of the extragalactic background light (EBL). Our data agree with most earlier IGL estimates and with direct measurements in the far IR, but disagree strongly with direct estimates in the optical. Close agreement between our results and recent very high-energy experiments (H.E.S.S. and MAGIC) suggests that there may be an additional foreground affecting the direct estimates. The most likely culprit could be the adopted model of zodiacal light. Finally we use a modified version of the two-component model to integrate the EBL and obtain measurements of the cosmic optical background (COB) and cosmic infrared background of 24^{+4}_{-4} nW m^{-2} sr^{-1} and 26^{+5}_{-5} nW m^{-2} sr^{-1} respectively (48%:52%). Over the next decade, upcoming space missions such as *Euclid* and the *Wide Field Infrared Space Telescope* will have the capacity to reduce the COB error to <1%, at which point comparisons to the very high-energy data could have the potential to provide a direct detection and measurement of the reionization field.

Key words: cosmic background radiation – cosmological parameters – diffuse radiation – galaxies: statistics – zodiacal dust

Supporting material: figure set, FITS files

1. INTRODUCTION

The extragalactic background light, or EBL (McVittie & Wyatt 1959; Partridge & Peebles 1967a, 1967b; Hauser & Dwek 2001; Lagache et al. 2005; Kashlinsky 2006; Dwek & Krennrich 2013), represents the flux received today from a steradian of extragalactic sky. It includes all far-UV to far-IR sources of photon production since the era of recombination, and thereby encodes a record of the entire energy production history of the universe from ~380,000 yr after the Big Bang to the present day—see Wesson et al. (1987) and Wesson (1991) for an interesting digression regarding the EBL's relation to Olber's Paradox. By convention, the EBL is defined as the radiation received between 0.1 and 1000 μm (e.g., Finke et al. 2010, Domínguez et al. 2011; Dwek & Krennrich 2013; Khaire & Srianand 2015). This arises predominantly from starlight, light from AGNs, and dust-reprocessed light—with some minimal (<15%) contribution from direct dust heating due to accretion (Alexander et al. 2005; Jauzac et al. 2011). Photon production occurs not only at far-UV to far-IR wavelengths, but across the entire electromagnetic spectrum (e.g., the cosmic X-ray background, see Shanks et al. 1991; and the cosmic radio background, see de Oliveira-Costa et al. 2008). However, based on considerations of integrated energy (i.e., $\int_{z=0}^{z=1050}\int_{\nu_1}^{\nu_2} \nu f_\nu\ \delta\nu\ \delta z$), the cosmic emission is dominated, in terms of newly minted photons, by the range from the far UV to far IR. The integrated EBL is smaller by a factor of ~20 than the cosmic microwave background (CMB), despite the $(1+z)^4$ diminution of the CMB photon energies, but is more than a factor of ×100 brighter than the other backgrounds. Putting aside the CMB and the pre-recombination universe, the EBL is a product of the dominant astrophysical processes that have taken place over the past 13 billion years, in terms of energy redistribution (baryonic mass → photons). In particular, because of the expansion, the precise shape of the spectral energy distribution of the EBL depends on the history of cosmic star formation, the history of AGN activity, and the evolution of dust properties over cosmic time. It therefore represents rich territory for comparison to models of galaxy formation and evolution (e.g., Domínguez et al. 2011; Somerville et al. 2012; Inoue et al. 2013).

The EBL can be broken down into two roughly equal contributions from the UV–optical–near-IR and the mid- to far-IR wavelength ranges, respectively the cosmic optical background (COB, 0.1–8 μm) and the cosmic infrared background (CIB, 8–1000 μm; Dwek et al. 1998). Despite the different wavelength ranges, the COB and CIB ultimately derive from the same origin: star formation and gravitational accretion onto supermassive black holes. The COB represents the light from stars and AGNs that directly escapes the host system and

[5] Present address: (SUPA) School of Physics and Astronomy, University of St Andrews, North Haugh, St Andrews KY16 9SS, UK.

proceed to pervade the intergalactic medium. The CIB represents that component which is first attenuated by dust near the radiation sources, and subsequently re-radiated in the mid and far IR. The nearly equal balance between the energies of the integrated COB and CIB is very much a testimony to the severe impact of dust attenuating predominantly UV and optical photons, particularly given the very modest amount of baryonic mass in the form of dust (<1% relative to stellar mass, see for example Driver et al. 2008; Dunne et al. 2011).

Previous measurements of the EBL have been of two types: direct measurements (e.g., Puget et al. 1996; Dwek & Arendt 1998; Fixsen et al. 1998; Hauser et al. 1998; Lagache et al. 1999; Cambrésy et al. 2001; Bernstein et al. 2002; Matsumoto et al. 2005, 2011; Dole et al. 2006; Bernstein 2007) and integrated galaxy counts (e.g., Madau & Pozzetti 2000; Totani et al. 2001; Xu et al. 2005; Dole et al. 2006; Hopwood et al. 2010; Keenan et al. 2010; Berta et al. 2011; Béthermin et al. 2012). These two methods should converge if the EBL is predominantly derived from galaxies (including any AGN component) and if the photometric data used to detect these galaxies are sufficiently deep.

Until fairly recently, insufficient deep data existed to completely resolve the EBL using galaxy number-counts, and direct measurements appeared to be the more compelling constraint. However, with the advent of space-based facilities (*GALEX*, *Hubble Space Telescope* (*HST*), *Spitzer*, and *Herschel*) and large ground-based facilities (VLT, Subaru), deep field data have now been obtained across the entire range from far UV to far IR. The comparison of the direct estimates and integrated number-counts is proving fertile ground for debate. In the CIB, the direct estimates agree reasonably well with the integrated source counts, which account for over 75% of the directly measured CIB (see Béthermin et al. 2012; Magnelli et al. 2013). The remaining discrepancy can be readily reconciled from extrapolations of the source counts, plus some additional contribution from lensed systems (Wardlow et al. 2013). In the optical and near IR the situation is less clear, with many direct estimates being a factor of five or more greater than the integrated galaxy counts (see for example the discussion on the near-IR background excess in Keenan et al. 2010 or Matsumoto et al. 2015), despite the advent of very wide and deep data. Either the integrated source counts are missing a significant quantity of the EBL in a diffuse component or the direct measures are overestimated (i.e., the backgrounds are underestimated).

Recently a third pathway to the EBL has opened up, via the indirect attenuation of TeV photons emanating from blazars, as observed with very high-energy (VHE) experiments (e.g., the High Energy Stereoscopic System, H.E.S.S., and the Major Atmospheric Gamma Imaging Cerenkov telescope, MAGIC). Here the TeV flux from a distant blazar, believed to exhibit a well behaved power-law spectrum, interacts with the intervening EBL photon field. Preferential interactions between TeV and micron photons create electron–positron pairs, thereby removing power from the received TeV spectrum over a characteristic wavelength range. The proof of concept was demonstrated by Aharonian et al. (2006) and comprehensive measurements have recently been made by both the H.E.S.S. Consortium (H.E.S.S. Collaboration et al. 2013) and the MAGIC team (Ahnen et al. 2016). These two independent measurements very much favor the low-EBL values. However, uncertainty remains as to the strength, and hence impact, of the intergalactic magnetic field, the intrinsic shape of the blazar spectrum, and the role of secondary PeV cascades. Moreover, the two VHE studies mentioned above require a predefined EBL model, and use the shape of the received TeV signal compared with the assumed intrinsic spectrum to provide a normalization point. Hence spectral information is essentially lost. Trickier to determine but more powerful is the potential for the VHE data to constrain both the normalization *and* the shape of the EBL spectrum. A first effort was recently made by Biteau & Williams (2015), who again found results consistent with the low-EBL value, but perhaps more crucially provided independent confirmation of the overall shape across the wavelength range from the far UV to far IR. Nevertheless, caveats remain as to the true intrinsic slope of the blazar spectrum in the TeV range, contaminating cascades from PeV photons, the strength of any intervening magnetic fields, and in some cases the actual redshift of the blazars studied.

Here we aim to provide the first complete set of measurements of integrated galaxy light based on a combination of panchromatic wide and deep number/source-count data from a variety of surveys that collectively span the entire EBL wavelength range (0.1 μm–1000 μm). Our approach varies from previous studies in that we abandon the concept of modeling the data with a model of galaxy counts (backward propagation). Instead, as the number-count data are bounded in all bands—in terms of the contribution to the integrated luminosity density—we elect to fit a simple spline to the luminosity density data.

In Section 2, we present the adopted number-count data, the trimming required before fitting, and estimates of the cosmic (sample) variance associated with each data set. In Section 3, we describe our fitting process and the associated error analysis. We compare our measurements to previous estimates in Section 4, including direct and VHE constraints, before exploring possible sources of missing light. We finish by using the EBL model of Driver & Andrews (see Driver et al. 2013; S. K. Andrews et al. 2016, in preparation) as an appropriate fitting function to derive the total integrated energy of the COB and CIB.

All magnitudes are reported in the AB system, and where relevant we have used a cosmology with $\Omega_\Lambda = 0.7$, $\Omega_{\rm Matter}= 0.3$, and $H_0 = 70\,{\rm km\,s^{-1}\,Mpc^{-1}}$.

2. NUMBER-COUNT DATA

This work has been motivated by the recent availability of a number of panchromatic data sets that extend from the far UV to the far IR. In particular, these are from the Galaxy And Mass Assembly (GAMA, Driver et al. 2011, 2016; Hopkins et al. 2013; Liske et al. 2015), COSMOS/G10 (Davies et al. 2015; Andrews et al. 2016), *HST* Early Release Science (ERS, Windhorst et al. 2011), and the *HST* Ultraviolet Ultra-Deep Field (UVUDF; Teplitz et al. 2013, Rafelski et al. 2015). For each of these data sets great care has been taken to produce consistent and high-quality photometry across a broad wavelength range. We have been responsible for the production of the first three catalogs, with the fourth recently made publicly available. We describe the various data sets in more detail below.

2.1. Galaxy And Mass Assembly (GAMA)

GAMA represents a survey of five sky regions covering 230 deg^2 (Driver et al. 2011), with spectroscopic data to

$r = 19.8$ mag obtained from the Anglo-Australian Telescope (Liske et al. 2015). Complementary panchromatic imaging data come from observations via *GALEX* (Liske et al. 2015), SDSS (Hill et al. 2011), VISTA (Driver et al. 2016), *WISE* (Cluver et al. 2014), and *Herschel* (Eales et al. 2010, Valiante et al. 2016). The GAMA Panchromatic Data Release imaging (Driver et al. 2016) was made publicly available in 2015 August (http://gama-psi.icrar.org). The area of 180 deg^2 that makes up the three GAMA equatorial regions (G09, G12, and G15) has since been processed with the custom-built panchro matic analysis code LAMBDAR (Wright et al. 2016) to derive matched-aperture and PSF-convolved photometry across all bands. The Wright catalog is *r*-band-selected using SExtractor (Bertin & Arnouts 1996). The SExtractor-defined apertures are convolved with the appropriate point-spread function for each facility and used to derive consistent flux measurements in all other bands. Care is taken to manage overlapping objects and flux-share appropriately (see Wright et al. 2016 for full details). As part of the quality control process, all bright and all oversized apertures (for their magnitude) were visually inspected and corrected if necessary. The Wright catalog then uses these apertures to provide fluxes in the following bands: FUV/NUV, *ugri*, *ZYJHK*, *IRAC*-1/2/3/4, PACS 100/160, SPIRE 250/350/500. Number-counts are generated by binning the data within 0.5 mag intervals and scaling for the area covered. Random errors are derived assuming Poisson statistics (i.e., $\sqrt{n}$) with cosmic variance errors included in the analysis as described in Sections 2.5 and 3.3.4. Note that in generating number-counts, the *r*-band selection will lead to a gradual flattening of the counts in other bands, particularly those bands furthest in wavelength from *r*, i.e., a color bias. The very simple strategy we adopt here is to identify the point at which the counts in the GAMA Wright catalog diverge from the deeper data sets and truncate our counts 0.5 mag brightward of this limit. See Wright et al. (2016) for full details of the GAMA analysis, including aperture verification.

2.2. COSMOS/G10

COSMOS/G10 represents a complete reanalysis of the available spectroscopic and imaging data to GAMA standards, in a 1 deg^{2}region of the *HST* COSMOS field (Scoville et al. 2007), dubbed G10 (GAMA 10^h; see Davies et al. 2015, Andrews et al. 2016 for full details). The primary source detection catalog uses SExtractor applied to deep Subaru *i*-band data, following trial-and-error optimization of the SExtractor detection parameters. All anomalous apertures were manually inspected and repaired as needed. As for GAMA, the LAMBDAR software was used to generate matched-aperture photometry from the far UV to far IR. The photometry for the COSMOS/G10 region spans 38 wavebands and combines data from *GALEX* (Zamojski et al. 2007), CFHT (Capak et al. 2007), Subaru (Taniguchi et al. 2007), VISTA (McCracken et al. 2012), *Spitzer* (Sanders et al. 2007; Frayer et al. 2009), and *Herschel* (Levenson et al. 2010; Lutz et al. 2011; Oliver et al. 2012; Smith et al. 2012; Viero et al. 2013; Wang et al. 2014). As for GAMA the number-counts are derived in 0.5 mag bins yielding counts in FUV/NUV, *u*, *griz*, YJHK, *IRAC*1/2/3/4, MIPS 24/70, PACS 100/160, SPIRE 250/350/500. The COSMOS/G10 catalog is *i*-band-selected, and hence a gradual decline in the number-counts will occur in filters other than *i*, as either very red or blue galaxies are preferentially lost. In particular, a cascading flux cut was implemented as the optical priors were advanced into the far IR to minimize erroneous measurements. As for GAMA we use the departure of the COSMOS/G10 counts from the available deeper data to identify the magnitude limits at which the counts become incomplete. See Andrews et al. (2016) for full details of the COSMOS/G10 analysis including data access.

2.3. Hubble Space Telescope Early Release Science (HST ERS)

The *HST* ERS data set (Windhorst et al. 2011) represents one of the first fields obtained using *HST*'s WFC3, and built upon earlier optical ACS imaging of the GOODS South field. Details of the analysis are provided in Windhorst et al. (2011), and counts are derived in 11 bands: F225W, F275W, F306W, F435W, F775W, F850LP, F098M, F105W, F125W, F140W, and F160W, covering 40–50 arcmin^2 to AB 26.3–27.5 mag. For the *HST* ERS, data catalogs were derived independently in each band, hence avoiding any color bias. *Spitzer* and *Herschel* data exist for the *HST* ERS field, but are currently not part of this analysis due to their much coarser beam and the resulting faint-end confusion. In due course, we expect to reprocess the ERS data using LAMBDAR. In addition to the *HST* ERS field the ASU team have also measured deep counts in various bands in the UDF and XDF fields using an identical process to that described for the *HST* ERS data, but including a correction for incompleteness by inserting false galaxy images into real data and assessing the fraction recovered as a function of magnitude. See Windhorst et al. (2011) for full details of the *HST* ERS and deep-field analysis.

2.4. Hubble Space Telescope Ultraviolet Ultra-deep Field (HST UVUDF)

The *HST* UVUDF data set (Teplitz et al. 2013) represents a major effort to bring together data on the HUDF field spanning a broad wavelength range and consisting of 11 bands from the near UV to the near IR (see Rafelski et al. 2015). The UVUDF team also use an aperture-matched method corrected for the point-spread function to derive the photometry. The area of coverage varies from 7.3 to 12.8 arcmin^2 across the bands. The initial detection image is derived from the combination of four optical and four near-IR bands (weighted by the inverse variance of each image on a pixel-by-pixel basis). Becasue the near-IR data are variable in depth, this does produce a catalog with a slightly variable detection wavelength. However, the basic strategy of object detection based on multi-filter stacked data combined with pixel weighting should mitigate most of the color selection bias in the count data. The catalog of Rafelski et al. is publicly available[6] and counts are derived by binning the data in 0.5 mag intervals and scaling for area. The *HST* UVUDF data set contains counts in the following bands: F225W, F275W, F336W, F435W, F606W, F775W, F850LP, F105W, F125W, F140W, and F160W. See Rafelski et al. (2015) for full details of the UVUDF data analysis.

2.5. Additional Data Sets and Cosmic Variance (CV)

In addition to the four primary catalogs mentioned above, we include a number of band-specific surveys to extend the range of our number-count analysis into the far UV, mid IR, and far IR. These data sets, along with the four primary data sets, are summarized in Table 1. All data sets will be susceptible to

[6] http://uvudf.ipac.caltech.edu/

cosmic variance, particularly at the fainter ends of the *HST* data sets, where the volumes probed will be very small. For each data set we therefore derive a cosmic (sample) variance error, listed in Column 5 of Table 1 using Equation (4) from Driver & Robotham (2010). These values are based on the quoted field of view, the number of independent fields, and an assumed redshift distribution, and the adopted values are also shown in Table 1. We refer the curious reader to our online calculator: http://cosmocalc.icrar.org (see Survey Design tab).

2.6. Merging Data Sets

Figure 1 shows the combined galaxy number-counts in the *r* band from six data sets of varying areas and depths. The figure highlights the distinct limits of each data set reflected by the abrupt downturns. Care must therefore be taken to truncate each data set at an appropriate magnitude limit. For the GAMA and COSMOS/G10 data sets we identify the downturn as the point at which the data become inconsistent with the deeper data sets. This is because the color bias introduces a shallow rather than abrupt downturn. For all other data sets we identify the point at which the counts at faint magnitudes fall abruptly, and then truncate 0.5 mag brightward. Truncating in this way results in a fairly seamless distribution (see Figure 2, top left panel).

Our final number-count distributions, for three arbitrarily selected bands (*r*, *IRAC*-1, and SPIRE 250 μm), are shown in Figure 2 (left panels). Following the trimming process, the data sets shown overlap extremely well.

Finally, the reader will notice that data contributing to the number-counts in some bands are determined through non-identical filters. Perfect color corrections to a single bandpass would require individual fitting of the spectral energy distribution, which itself is imprecise, and the corrections of the mean of the data will in all cases be less than ± 0.05 mag. Given the very good agreement between our counts, despite slight filter discrepancies, we elect to assume that these offsets do not significantly affect our derived results, and to instead fold an additional systematic error of 0.05 mag into our EBL error analysis (see Section 3.3.1).

3. THE FAR-UV–FAR-IR EXTRAGALACTIC BACKGROUND LIGHT

To derive a measurement of the extrapolated integrated galaxy count (eIGL) from data on galaxy counts, one typically constructs a model of galaxy number-counts tailored to match the data. One can then integrate the luminosity-weighted model either to the limit of the data (providing a lower limit) or to the limit of the model (an extrapolated measurement). In practice, these measures are referred to as integrated galaxy light (IGL) measurements, and in the absence of other significant sources of radiation, they should equate to the true EBL. Here, we deviate from this path in two ways. First, we elect to simply fit a 10-point spline to the available data; second, we directly fit to the luminosity-weighted data rather than the number-counts. These two departures are intended to provide a more robust measurement because the spline should map the nuances of the data perfectly, while number-count models are inevitably imperfect. In the event that the distributions are well bounded by the data in terms of their contribution to the IGL, the nonphysical nature of the extrapolation is not particularly significant.

3.1. Spline Fitting

We derive our values of luminosity density via spline fitting, using the R[7] SMOOTH.SPLINE routine with 10 degrees of freedom (spline points). In fitting the spline the data points are weighted in inverse proportion to σ^2. To derive our IGL estimates we use the spline fit to populate a differential distribution of luminosity density from AB $= -100$ to AB $= 100$ mag in intervals of 0.01 mag and then sum the predicted values (dividing by the bin width). In all cases, flux outside the summing range is negligible. Where data sets overlap in a particular magnitude interval, our spline fits will be driven by the survey with the largest area coverage because the fitting process is error-weighted ($1/\sigma^2$). Hence, the significance of the fit will progress from data drawn from 180 deg^2 for GAMA at the brightest end, through 1 deg^2 for the COSMOS/G10 region, to 40 arcmin^2 for the *HST* ERS data and 10 arcmin^2 for the deepest *HST* UDF data. This progression of area and depth highlights the importance of combining both wide and deep data sets in this way. Number-count data for the FUV/NUV, *ugi*, *ZYJHK*, *IRAC* 124, MIPS24, *Herschel* PACS 70/100/160, and SPIRE 250/350/500 bands are shown in Figure Set 8. In all cases, the number-count data are consistent across the data sets within the quoted errors following the above trimming process.

3.2. Measurements of the EBL

Figure 2 (right panels) shows the contribution within each magnitude interval to the luminosity density (data points as indicated) for the *r*, *IRAC*-1, and SPIRE 250 μm bands. Overlaid is the best-fit spline model (black curve). Beyond the data range, the extrapolation of the spline fit is shown as red dashed lines. Also shown, as gray lines, are spline fits to perturbations of the data as described in Section 3.3.3. Note that the units we adopt for the far-IR data will be unfamiliar to the far-IR community used to working in Euclidean normalized source counts in intervals of jansky. Here, for consistency, we have elected to process and show all data in the traditional optical units of AB magnitude intervals. Figure Set 8 (right panels) shows the luminosity density fits in the remaining 18 bands. In all cases the data are bounded (right panel), i.e., the contribution to the luminosity density rises to a peak and then decreases with increasing magnitude (decreasing flux). This implies that the dominant contribution to the IGL is resolved, and that adopting a spline-fitting approach rather than the approach of a galaxy number-count model is reasonable. The only possible exception is the *IRAC*-4 data, where the peak is only just bound (see Figure A1.12, right panel).

In Table 2 we present three distinct measurements. The first (Column 3) is our best-fit eIGL values based on a spline fit to the data. We also present the median value from 10,001 Monte Carlo realizations (Column 4) as discussed in Section 3.3.3. In all cases, the best-fit and median estimates agree extremely closely, as one would expect. In Column 5 we present the measurement of the IGL, but confine ourselves to the range covered by the data, i.e., no extrapolation. This will naturally provide a lower limit, and a comparison between the values in Column 3 and Column 5 provides some indication of where the extrapolation is important for measuring the eIGL. In most cases (see Figure 3, gray dotted lines), comparisons between

[7] R Core Team (2015). R: A language and environment for statistical computing, R Foundation for Statistical Computing, Vienna, Austria: https://www.R-project.org/.

Table 1
Summary of Data Sets Used in This Analysis

Filter	Description	Ω (deg^2)	z range	CV	Reference
All	GAMA 21 band panchromatic data release	3 × 60	0.05–0.30	5%	Wright et al. (2016)
All	COSMOS/G10 38 band panchromatic data release	1	0.2–0.8	11%	Andrews et al. (2016)
UV–NIR	*HST* WFC3 Early Release Science (Panchromatic Counts)	0.0125	0.5–2.0	17%	Windhorst et al. (2011)
UV–NIR	*HST* Ultraviolet through NIR observations of the Hubble UDF	0.0036	0.5–2.0	21%	Rafelski et al. (2015)
FUV	*HST* ACS Solar Blind Channel observations of HDF-N (GOODS-S), HUDF, GOODS-N	3 × ∼0.0015	0.5–2.0	14%	Voyer et al. (2011)
NUV	STIS observations in the HDF-N, HDF-S, and the HDF-parallel	3 × ∼0.00012	0.5–2.0	21%	Gardner et al. (2000)
u	Near-UV (360nm) observations in the Q0933+28 field with the Large Binocular Camera	0.4	0.5–2.0	8%	Grazian et al. (2009)
K	The Hawk-I UDS and GOODS Survey (HUGS)	0.016, 0.078	0.5–2.0	11%	Fontana et al. (2014)
IRAC-1/2	S-CANDELS: The Spitzer–Cosmos Assembly Near Infrared Deep Extragalactic Survey: 3.6 and 4.5 μm *Spitzer* IRAC	5 × ∼0.032	0.5–2.0	6%	Ashby et al. (2015)
IRAC-4 (8 μm)	*Spitzer* IRAC Band 4 data of the EGS field	0.38	0.5–2.0	8%	Barmby et al. (2008)
24 μm	*Spitzer* MIPS 24 μm observations of Marano, CDF-S, EGS, Boötes, and ELAIS fields	0.36,0.58,0.41, 9.0,0.036	0.5–2.0	3%	Papovich et al. (2004)
24 μm	*Spitzer* MIPS 24 μm data in FIDEL, COSMOS, and SWIRE fields	53.6 (nine fields)	0.5–2.0	2%	Béthermin et al. (2010)
70/160 μm	*Spitzer* MIPS 70 and 160 μm data	45.4 (nine fields)	0.5–2.0	2%	Béthermin et al. (2010)
70 μm	*Herschel* PACS 70 μm data	42.9 (nine fields)	0.5–2.0	2%	Béthermin et al. (2010)
100/160 μm	*Herschel*: The PACS Evolutionary Probe Survey (100 and 160 μm data) of the GOODS-S, GOODS-N, Lockman Hole, and COSMOS areas	0.083,0.083,0.18, 2.04	0.5–2.0	5%	Berta et al. (2011)
100/160 μm	*Herschel*: PACS 100 and 160 μm data from PEP and GOODS–*Herschel* campaigns	2 × ∼0.052	0.5–2.0	9%	Magnelli et al. (2013)
250/350/500 μm	*Herschel* (HerMES) SPIRE 250, 350, and 500 μm observations in the COSMOS and GOODS-N regions	0.083, 2.04	0.5–2.0	5%	Béthermin et al. (2012)
250/350/500 μm	*Herschel* (H-Atlas) SPIRE 250, 350, and 500 μm observations in the equatorial GAMA fields	3 × 54	0.05–2.0	2%	Valiante et al. (2016)

Note. The table summarizes the data sets used in this analysis and in particular the cosmic variance errors estimated via Equation (4) from Driver & Robotham (2010); see also http://cosmocalc.icrar.org for our online calculator.

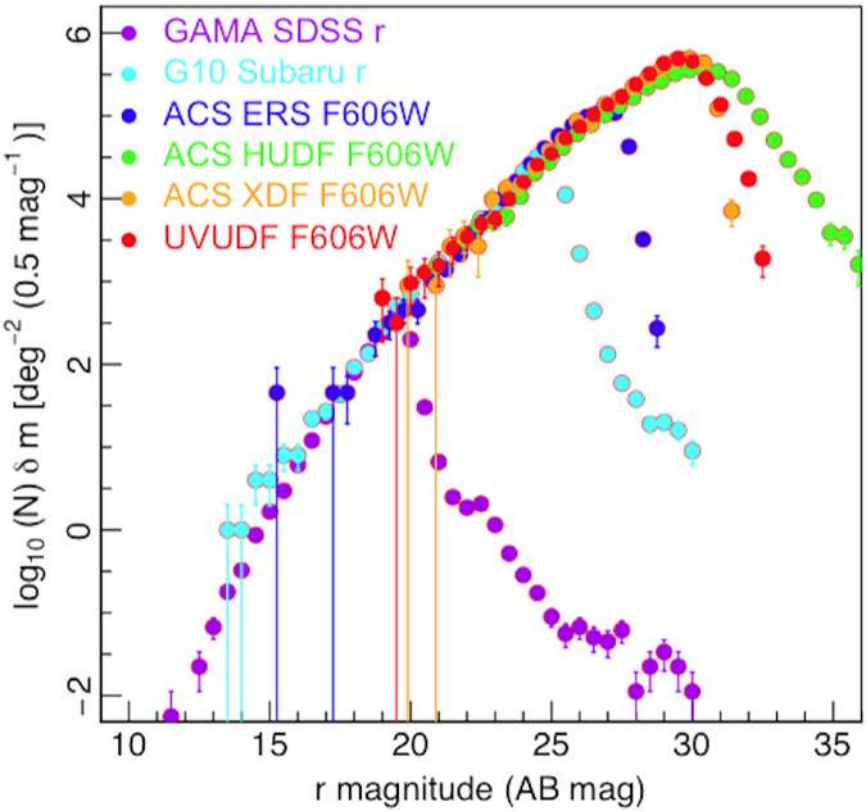

Figure 1. *r*-band number-counts produced by simply combining the catalogs as provided. Each data set shows a clear downturn in the number-counts at faint magnitudes, which is an artifact of the flux and color limit of that data set. To correct for this, we truncate each data set 0.5 mag brightward of its downturn point. In some cases we also truncate bright data, when the error bars become excessive, but this has no impact on our fitting.

the lower limit and extrapolated values suggest that <5%–10% of the COB measurements derive from these extrapolations, and typically <20%–30% for the CIB. Although the spline fit is not physically motivated, the figures show that the fits behave sensibly, and that the extrapolations project linearly beyond the range of the data points. However, as the underlying number-count data are generally flattening (because of the diminishing volume for higher-z systems due to the cosmological expansion), this does lead to the possibility of a small overestimate in our eIGL measurements, albeit well within the quoted errors. Hence, the most cautious way to interpret our analysis would be to adopt the range that extends from the lower limit from the non-extrapolated values (minus the error) to the eIGL (plus the error).

Table 3 provides an extract of our trimmed data listing our compiled number-counts and associated errors, as used for our spline fitting for each waveband. This data file is available online in FITS format.

3.3. Appropriate Error Estimation

There are a number of possible sources of error; in particular we consider those arriving from a systematic photometric error (zero-point shift or background over/underestimation), the fitting process, those implied from the errors in the count data, and the possible impact of cosmic variance. We explore each of these in turn.

3.3.1. Photometric Error

In most cases where we have multiple data sets we see that the counts agree within 0.05 mag, despite the potential for filter offsets due to small bandpass discrepancies. Generally, errors in absolute zero-points, particularly in *HST* data, are expected to be <0.01–0.02 mag. However, the process of sky subtraction, object detection, and photometric measurement can lead to significant *systematic* variations. The easiest way to quantify the impact is to *systematically* shift all data sets by ±0.05 mag and re-derive our measurements. The value of ±0.05 mag comes from the amount required to align the various deep data sets, and is taken here to represent the systematic uncertainty in the entire photometric extraction process. This level of uncertainty should be considered conservative—surveys such as GAMA, for example, typically quote errors of ±0.03 in photometric measurements—but high-z galaxies are often asymmetric, and their photometry is distorted by ambiguous deblends. Hence, a larger assumed error of ±0.05 mag seems plausible and prudent. Column 6 of Table 2 shows the perturbation to the best-fit value if all data points are systematically shifted by ±0.05 mag. Only for MIPS 24 μm does this error dominate (Figure 3, green line).

3.3.2. Spline Fitting Error

The fitting process we adopt arbitrarily uses a 10-point spline fit. This was judged to be the lowest number of spline points required to represent the data well. We repeat our analysis using an 8- or 12-point spline fit and report the impact (Column 7) on our best-fit value using these alternative representations, i.e., $|\Delta\rho_L|/2$. In all cases except for *IRAC*-4, where other issues have already been raised, the variation due to the fitting process is negligible (Figure 3, red line).

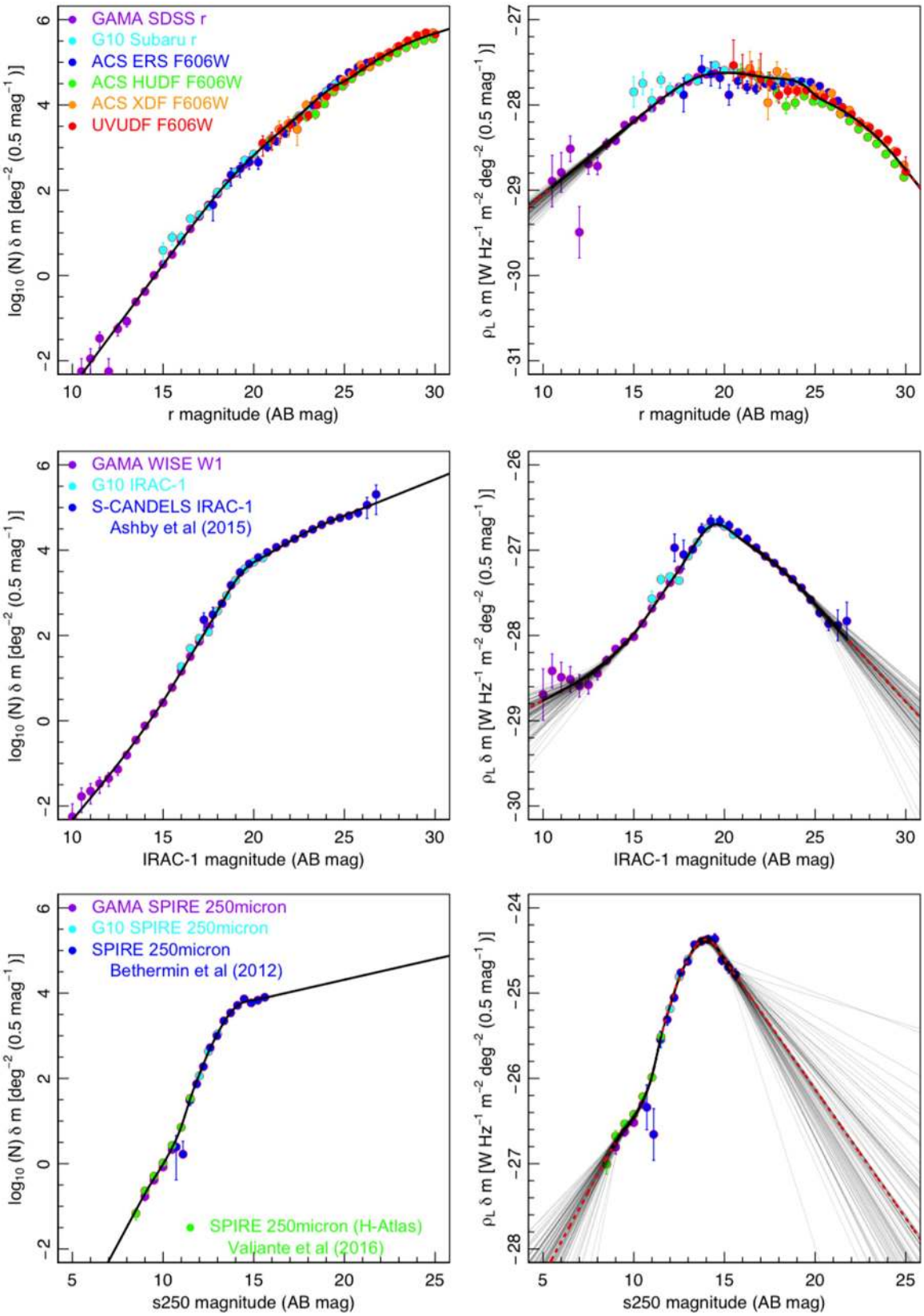

Figure 2. Left: galaxy number-counts in the specified band, where the black curve depicts the 10-point spline fit to the luminosity density data. Right: the contribution of each magnitude interval to the luminosity density. Where the spline fit is extrapolated this is shown as a red dashed line. Also shown are 101 faint gray lines indicating identical fits to data randomly perturbed within their errorbars.

Table 2
Measurements of the eIGL

Filter Name	Pivot Wavelength (μm)	Extrapolated IGL (Best-fit)	Extrapolated IGL (Median)	IGL Lower Limit (nW m^{-2} sr^{-1})	Zero-point Error	Fitting Error	Poisson Error	CV Error
(1)	(2)	(3)	(4)	(5)	(6)	(7)	(8)	(9)
FUV	0.153	1.45	1.45	1.36	±0.07	±0.00	±0.04	±0.16
NUV	0.225	3.15	3.14	2.86	±0.15	±0.02	±0.05	±0.45
u	0.356	4.03	4.01	3.41	±0.19	±0.04	±0.09	±0.46
g	0.470	5.36	5.34	5.05	±0.25	±0.04	±0.05	±0.59
r	0.618	7.47	7.45	7.29	±0.34	±0.05	±0.04	±0.69
i	0.749	9.55	9.52	9.35	±0.44	±0.00	±0.05	±0.92
z	0.895	10.15	10.13	9.98	±0.47	±0.03	±0.05	±0.96
Y	1.021	10.44	10.41	10.23	±0.48	±0.00	±0.07	±1.05
J	1.252	10.38	10.35	10.22	±0.48	±0.00	±0.05	±0.99
H	1.643	10.12	10.10	9.99	±0.47	±0.01	±0.06	±1.01
K	2.150	8.72	8.71	8.57	±0.40	±0.02	±0.04	±0.76
IRAC-1	3.544	5.17	5.15	5.03	±0.24	±0.03	±0.06	±0.43
IRAC-2	4.487	3.60	3.59	3.47	±0.17	±0.02	±0.05	±0.28
IRAC-4	7.841	2.45	2.45	1.49	±0.11	±0.77	±0.15	±0.08
MIPS24	23.675	3.01	3.00	2.47	±0.14	±0.05	±0.06	±0.07
MIPS70	70.890	6.90	6.98	5.68	±0.32	±0.07	±0.79	±0.18
PACS100	101.000	10.22	10.29	8.94	±0.47	±0.10	±0.56	±0.88
PACS160	161.000	16.47	16.46	10.85	±0.76	±0.81	±2.99	±1.57
PACS160[a]	161.000	13.14	9.17	8.93	±0.61	±0.17	±1.32	±0.72
SPIRE250	249.000	10.00	10.04	8.18	±0.46	±0.18	±0.87	±0.59
SPIRE350	357.000	5.83	5.87	4.66	±0.27	±0.24	±1.04	±0.32
SPIRE500	504.000	2.46	2.48	1.71	±0.11	±0.03	±2.54	±0.13

Note. Measurements of the eIGL are from integrating spline fits to the luminosity-weighted number-counts (Column 3) and from the median of our 10,001 Monte Carlo realizations (Column 4). Lower limits to the eIGL are from integrating within the data range only (Column 5), and errors (associated with zero-point uncertainty, fitting methodology, and from Monte Carlo realizations of the random or CV errors (Columns 6, 7, and 8 respectively), all at the wavelengths indicated by the bandpass or pivot wavelength indicated in Columns 1 or 2, respectively.
[a] Refitted excluding the very faint number-count data of Magnelli et al. (2013) where the completeness corrections exceed ×1.2.

3.3.3. Poisson Error

To assess the error arising from the uncertainty in the individual data points, we conduct 10,001 Monte Carlo realizations where we randomly perturb each data point by its permissible error, assuming the errors follow a normal distribution. For each sequence of perturbations we refit the spline and extract the values of the 16th percentile and the 84th percentile for the luminosity density. The uncertainty given in Column 7 of Table 2 is then $|\Delta\rho_L|/2$. We see that this error becomes dominant for data longwards of MIPS 24 μm (Figure 3, blue line).

3.3.4. Cosmic Variance Error

Finally we assess the error introduced by cosmic variance (or sample variance), as discussed by Driver & Robotham (2010). For each data set shown in Table 1, we derive and assign an estimate of cosmic variance based on Equation (4) in Driver & Robotham (2010), using the appropriate areas of the various data sets and some assumption of the likely redshift range contributing to the counts (see Table. 1). We conduct 10,001 Monte Carlo realizations, where we perturb each data set by a random amount defined by its cosmic variance (assuming the CV offset can be drawn from a normal distribution). We extract the 16th percentile and the 84th percentiles, from which we derive an uncertainty, as $|\Delta\rho_L|/2$. We see from Figure 3 (orange line) that this error dominates for most of the UV, optical, near-IR, and mid-IR bands.

3.3.5. Combining Errors

Combining random and systematic errors is not entirely straightforward, with some proponents advocating simply adding them while others prefer adding in quadrature or keeping the systematic and random errors separate. Here we take the most conservative approach of adding the errors linearly, but provide the individual errors in Table 2 for those wishing to combine them in other ways. The data points shown on subsequent figures are calculated according to $\Delta_{\rm Total} = \Delta_{\rm Col.6} + \Delta_{\rm Col.7} + \Delta_{\rm Col.8} + \Delta_{\rm Col.9}$.

Figure 3 shows the contribution of each of the individual errors to our eIGL measurements and highlights the transition from being dominated by cosmic variance error at shorter wavelengths to random errors at longer wavelengths. At one wavelength (*IRAC*-4), we note that the fitting error itself dominates because of the complex shape of the data. One clear consequence from Figure 3 is that deep, wide data are essential to reduce this error component, which should be readily achievable in the optical and near IR, with the upcoming *Euclid* and *Wide Field Infrared Space Telescope (WFIRST)* space missions. Assuming calibration errors can be minimized, there is the distinct possibility of obtaining eIGL measurements to better than 1% over the next decade.

3.4. Comparison to Previous EBL and eIGL Measurements

Figure 4 shows various IGL and EBL measurements as reported over the past few years. Most of the data come from the comprehensive compilation by Dwek & Krennrich (2013)

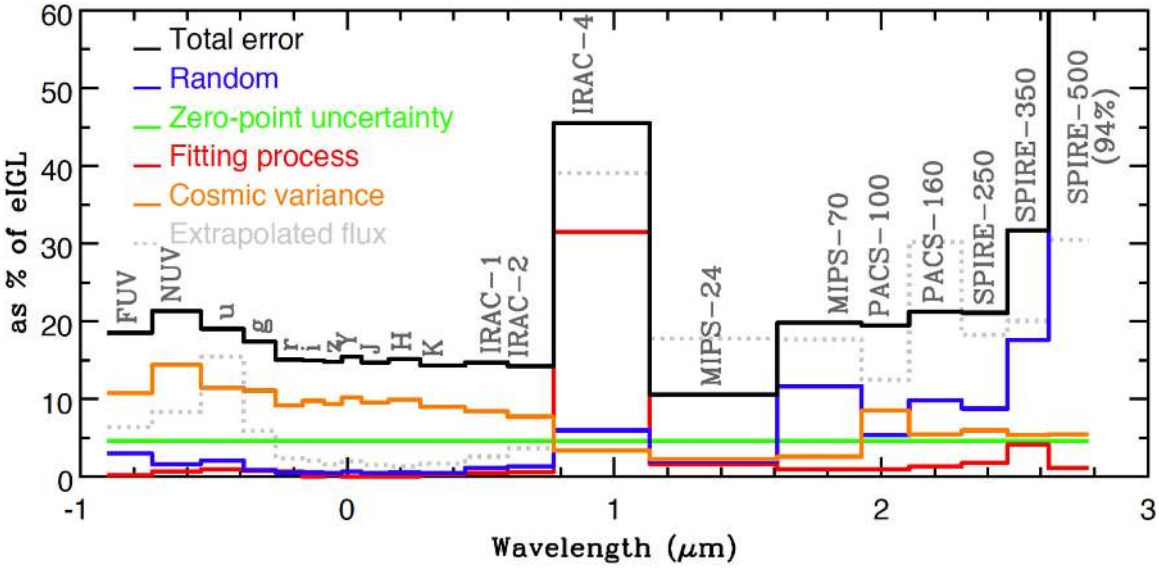

Figure 3. The contribution of each of the individual errors as a percentage of the eIGL measurement as a function of wavelength (as indicated). The black line shows the total error, which is mostly dominated by cosmic variance in the optical, near-IR, and mid-IR bands but by random errors in the far-IR band.

Table 3
The Compendium of Galaxy Number-counts in 21 Bands Assembled from Various Sources and Contained in One FITS File

Facility Name	Filter Name	Mag. Bin Center (mag)	$N(m)$ (0.5 mag^{-1} deg^{-2})	$\Delta N(m)$ (0.5 mag^{-1} deg^{-2})	Seq. No.	CV (%)	Reference
GALEX	FUV	14.0	0.01331	0.00941	1	5	Wright et al. (2016)
GALEX	FUV	14.5	0.01331	0.00941	1	5	Wright et al. (2016)
GALEX	FUV	15.0	0.01996	0.01152	1	5	Wright et al. (2016)
Herschel	SPIRE500	14.8586	4107.05	617.418	3	5	Béthermin et al. (2012)
Herschel	SPIRE500	15.2244	4898.7	735.368	3	5	Béthermin et al. (2012)
Herschel	SPIRE500	15.612	5556.47	1385.51	3	5	Béthermin et al. (2012)

Note. A sample of the first and last three lines of the data file is shown here. Columns 1 and 2 indicate the facility and filter from which the data are derived. Column 3 shows the magnitude bin center, Column 4 the number-counts within that bin, and Column 5 the error as provided. Column 6 refers to the data set number for that filter, Column 7 the cosmic variance as shown in Table 1, and Column 8 the literature reference for the data.
(This table is available in its entirety in FITS format.)

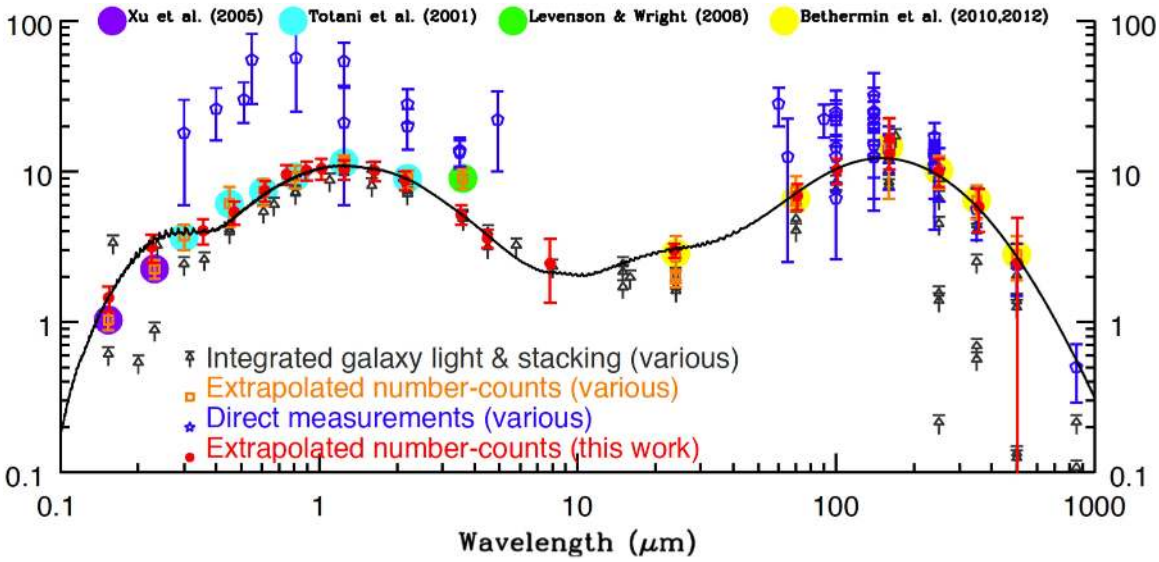

Figure 4. Our measurement of the eIGL based on extrapolated number-counts in each band compared to literature measurements taken from Dwek & Krennrich (2013). The black line depicts a phenomenological model from S. K. Andrews et al. (2016, in preparation). The blue data points are attempted direct measurements that require accurate modeling of both the Milky Way and zodiacal light.

(see their Tables 3–5 for detailed references, although most appear here in the introduction and text), plus more recent measurements by Ashby et al. (2015). We color-code the data into three sets following Dwek & Krennrich: lower limits on the IGL (gray), IGL measurements based on various extrapolated number-counts (orange), and direct measurements of the EBL via various methods (blue). Our new data are shown in red and appear consistent with most previous eIGL measurements. Within the eIGL data we see only one major discrepancy, which is with the value of Levenson & Wright (2008) in the *IRAC*-1 band. We find a significantly ($\times 2$) lower value. Levenson & Wright (2008) also combine data on galaxy counts from a number of sources and use two methods for deriving photometry—profile fitting and apertures. Both require significant corrections (upward shifts of ~40%). The value reported is from profile fitting, but we note that their corrected-aperture value is significantly lower (5.9 ± 1.0 nW m^{-2} sr^{-1}) and consistent with our measurement (5.2 ± 0.8 nW m^{-2} sr^{-1}). We argue that, as our 3.6 μm measurement lies in between our 2.2 and 4.6 μm measurements, it is likely that the profile-fit value of Levenson & Wright (2008) is biased high.

In the far UV and near UV, we recover higher measurements than those reported by Xu et al. (2005), although formally at the 1σ error limits. However, this is nonetheless consistent with the data shown in Xu et al. (2005) (see their Figure 1) where their number-counts in both the far UV and near UV, to which their model is fitted, do appear to fall systematically below the comparison data sets. See also Figure 6 of Voyer et al. (2011), which shows an offset between the data of Xu et al. (2005) and Hammer et al. (2010). Table 2 of Voyer et al. (2011) reports eIGL measurements by Voyer et al. (2011) and Xu et al. (2005) as well as Gardner et al. (2000) and earlier studies. Our value agrees well with—in fact, lies between—the two estimates provided by Voyer et al. (2011). In the near UV our result is dependent on an entirely different data set, namely F225W observations of the UVUDF. These data are very different to the *HST* ACS SBC data of Voyer et al. (2011) and agree closely with the much earlier *HST* STIS data of Gardner et al. (2000). We therefore conclude that the UV excess seen in our data against the model is supported by three distinct data sets and therefore likely real and significant.

In the far IR, we see that our measurements mostly agree with those previously reported. The one obvious outlier is the PACS 160 μm data, but we note (see Table 2) that a significant amount of flux is coming from the extrapolation. In particular the deepest data points from Magnelli et al. (2013) do include significant completeness corrections. If we refit using only data with completeness corrections at $<20\%$ (their filled data points on their Figure 6), we recover a much more consistent value (see the second entry in Table 2 and orange data point on Figure 4). We therefore elect to adopt this revised data point as the more robust estimate.

Most apparent from Figure 4 is the discrepancy in the optical to near IR between all the eIGL data (including our own) and the direct measurements. This is in stark contrast to the far IR, where the eIGL and EBL measurements agree within the specific errors. In the case of the far IR, the agreement is reassuring, and the much smaller error bars on the eIGL measurements suggest that the eIGL route is the more robust. Why then do we see such a discrepancy in the optical? The model curve (black) shows the model of energy evolution reported in S. K. Andrews et al. (2016, in preparation), which agrees closely with the eIGL data. Both the model and the general consensus in the far IR would therefore suggest that the error may lie in the direct measurements, some of which do concur with the eIGL estimates. It is worth noting that direct measurements rely on a robust subtraction of the foreground light, of which there are two dominant sources: the stellar population of the Milky Way and zodiacal light (Hauser & Dwek 2001; Mattila 2006). That the discrepancy is most apparent at a wavelength comparable to the peak in the solar spectrum also suggests that one or both of these foregrounds is the source of the problem, and that either the Milky Way model or the zodiacal model has been underestimated. One indication for the latter over the former is the reanalysis of data taken between 1972 and 1974 at 0.44 μm and 0.65 μm by the *Pioneer 10/11* spacecraft (Matsuoka et al. 2011). During that period the spacecraft were approximately 4.66 AU away from the Sun, where the contribution from zodiacal light should be negligible. Matsuoka found significantly lower EBL measurements that are in agreement with our eIGL values. We advocate that, given this information, it might be useful to adopt the eIGL as the de facto measurements of the EBL, and use these to help improve the model of zodiacal light and dust in the inner solar system.

3.5. Comparison to Very High-energy Data

Figure 5 shows the comparison of our eIGL data to three VHE data sets (as indicated). The agreement is much better than with the direct estimates, and provides additional independent evidence that the direct estimates may be in error. Note that the H.E.S.S. and MAGIC data sets each adopt a predefined EBL model and solve for the normalization, hence the slight discrepancy in shape between the VHE and eIGL data is of no significance. Formally, the data sets overlap within the 1σ errors, although the error range of the VHE data is fairly broad ($\times 2$). As discussed in the introduction, the VHE data also come with some caveats, in particular the assumption of the intrinsic shape of the blazar spectra/spectrum and the possibility of other interactions, e.g., with the intergalactic magnetic field or with PeV cascades. Nevertheless, the agreement is extremely encouraging and, taken at face value, suggests that our eIGL measurements are close to the underlying EBL values.

3.6. Potential Sources of Missing Light

Before equating our eIGL measurement to the EBL we should first acknowledge, in particular, the possible contributions from the low-surface-brightness universe: those from intracluster and intragroup light (Zwicky 1951), also referred to as intrahalo light or IHL (Zemcov et al. 2014), and that from the epoch of reionization (Cooray et al. 2012).

3.6.1. Low-surface-brightness Galaxies

The space density of low-surface-brightness galaxies is currently poorly constrained; however, observations in the Local Group suggest that the luminosity density is very much dominated by the Milky Way and Andromeda. This picture is generally supported by our own estimates of the low-surface-brightness population from the *HST* HDF (Driver 1999) and the Millennium Galaxy Catalog (see Liske et al. 2003; Driver et al. 2005). Both studies explored the low-surface-brightness universe and, while finding numerous new systems, these

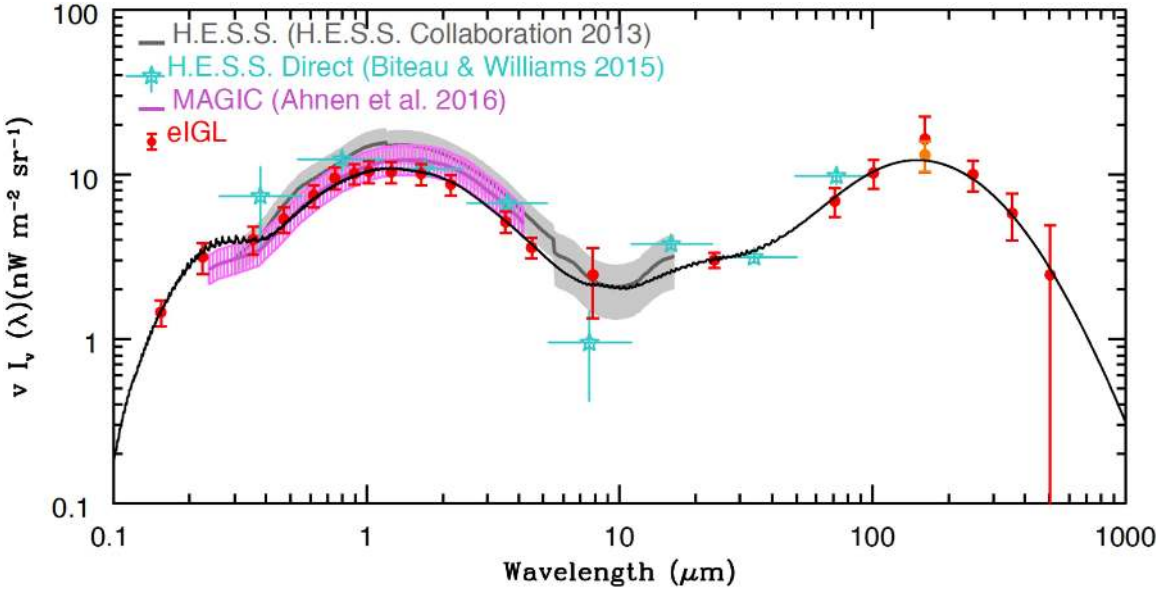

Figure 5. Our measurements of the eIGL along with the model of Andrews et al. compared to the available VHE data from the H.E.S.S. and MAGIC Consortium (both of which use a predefined EBL model). The blue stars show the VHE constraints by Biteau & Williams (2015) which are independent of any predefined EBL model.

systems ultimately contribute only small amounts of additional light (<20%; Driver 1999). Studies of rich clusters have also been very successful at finding low-surface-brightness systems (e.g., Davies et al. 2016; van Dokkum et al. 2015), yet not in sufficient quantities to significantly affect the total luminosity density, e.g., the thousand new galaxies found in the Coma cluster by Koda et al. (2015) collectively add up to just one extra L^* galaxy.

Two final arguments can be made for a minimal amount of missing light from low-surface-brightness galaxies based on the actual number-count and IGL data. First, as each survey would have a distinct cutoff in surface brightness, any large population would be truncated at different surface brightness levels, leading to stark mismatches between the distinct surveys. That the surveys overlap so well is a strong argument for any missing population being relatively modest in terms of its luminosity density. Second, any missing population of galaxies will contain both optical emission from the starlight and dust emission from reprocessed starlight. Hence the consistency between the far-IR EBL and eIGL can provide a constraint. To assess this we compare our values of the eIGL to the direct EBL measurements of Fixsen et al. (1998), and derive (eIGL/EBL) ratios of 0.96, 0.97, 1.05, and 1.03 in 160, 250, 350, and 500 μm bands for an average of 1.01, i.e., on average 100% of the direct EBL is "resolved" by our eIGL measurements.

This therefore gives no room for an upward adjustment for missing "dusty" galaxies. However, we do acknowledge that the errors in both our data and the data of Fixsen are significant (typically 40% per band), and hence this close agreement must be somewhat coincidental. Folding in the errors, there is potentially room for an ~19% upward adjustment, i.e., $40\%/\sqrt{4}$, before our eIGL exceeds the EBL measurements of Fixsen by their reported 1σ errors. Of course, this argument assumes that the dust properties of low-surface-brightness galaxies are consistent with those of normal spiral galaxies, which may not be the case. A similar conclusion, with regard to missing galaxy light, was also reached by Totani et al. (2001), who specifically explored the potential impact of selection by surface brightness in deep Subaru number-counts, and concluded that any impact from missing low-surface-brightness galaxies, via number-count modeling, was <20% in the *BVIJL* bands. Our range of 20% is comparable and hence we can adopt a possible range for upward adjustment of 0%–20% for missing low-surface-brightness galaxies.

3.6.2. Intracluster and Intragroup Light

The case for intracluster light is slightly less clear-cut. Mihos et al. (2005) shows spectacular images of nearby systems, including Virgo, which typically contain between 10% and 20% of the light in a diffuse component. In the Frontiers' cluster A2744, Montes & Trujillo (2014) find that the ICL makes up only 6% of the stellar mass. Similarly, the study by Presotto et al. (2014) also finds a relatively modest amount of mass (8%) in the CLASH-VLT cluster MACS J1206.2-0847. Earlier studies of Coma, perhaps the most studied system, found significantly more diffuse light, extending up to almost 50% (Bernstein et al. 1995), and simulations by Rudick et al. (2011) suggest that the ICL might contain anywhere from 10% to 40% of a rich cluster's total luminosity. Hence, studies of the ICL could be used to argue for an upward adjustment of the optical-only light of between 10% and 50%. However, it is important to remember that rich clusters, such as Coma, the Frontiers', and CLASH clusters are exceedingly rare (Eke et al. 2005), with less than 2% of the IGL coming from $>10^{14.5}\,M_{\odot}$ haloes (see Eke et al. 2005; S. P. Driver et al. 2016, in preparation).

In the absence of quality data, intuition can lead one in both directions, because the fraction of diffuse light is likely to be a function of the halo velocity dispersion, and the galaxy–galaxy interaction velocity, duration, and frequency. Certainly evidence from the Local Group suggests a fairly modest contribution, with the Magellanic Stream representing the only significant known source of diffuse light. Furthermore the deep study of M96 (Leo I group) by Watkins et al. (2014) failed to

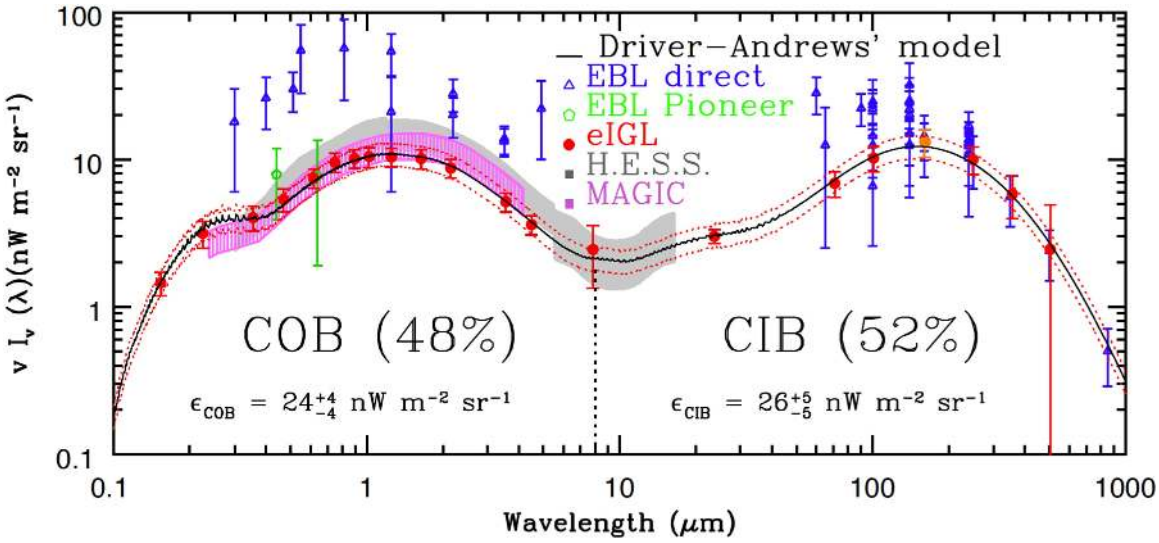

Figure 6. Our derived eIGL data (red points) compared to terrestrial and near-solar-system direct measurements (blue triangles) and the direct estimates from the *Pioneer* spacecraft at >4.5 AU (green circles). Also shown are the modified Driver–Andrews model (black line) and the error bounds (red dashed lines) adopted for determining the uncertainty in the integrated COB and CIB measurements (as shown).

identify any significant intragroup light to limits of 30.1 mag arcsec^{-2}.

Intrahalo light will only affect the optical bands because it is dust-free due to the UV flux pervading the intracluster medium and destroying any dust particles. We can therefore gauge the possible level by comparing our eIGL *g*-band measurement to the EBL. As mentioned earlier, because of uncertainties in the model of zodiacal light we cannot use most of the direct estimates, but we can use the values provided by Matsuoka et al. (2011) obtained from *Pioneer 10/11*. Using these, we find eIGL/EBL ratios of 0.68 ± 0.23 and 0.97 ± 0.43 in the *g* and *r* bands respectively (with the errors dominated by the uncertainty in the *Pioneer* estimates). The errors are large but suggest that the contribution from the IHL (which can only be positive) lies in the range 3%–32% but with a possible extreme upper limit of a ∼35% (i.e., $\frac{(0.68-0.23)+(0.97-0.43)}{2}\Big/\sqrt{2}$) upward correction of the optical and near-IR data (in line with our earlier discussion of the ICL).

3.6.3. Reionization

Reionization could potentially provide an additional diffuse photon field in the near-IR range, i.e., where Lyα is redshifted longward of 1 μm. Recent modeling by Cooray et al. (2012) suggests the flux of reionization today might be in the range 0.1–0.3 nW m^{-2} sr^{-1} at ∼1.1 μm, i.e., a 3% effect. This is well below our quoted errors and so reionization is unlikely to significantly impact upon our measurements. However, it is worth noting that the reionization models are uncertain, and a more rigid upper limit of ∼2 nW m^{-2} sr^{-1} at 1 μm was set by Madau & Silk (2005), based on arguments that related to the production of excessive metals if the reionizing flux was any stronger. This latter level is plausibly detectable and could cause our eIGL to underestimate the EBL by ∼20% in the near IR. Hence comparison of the near-IR eIGL to direct EBL measurements could conceivably detect the reionization field.

3.6.4. eIGL → EBL

The eIGL and the EBL are, from the discussion above, slightly different entities: the eIGL represents the sum of all radiation from bound galaxies while the EBL includes, in addition, diffuse light from the IHL and the epoch of reionization. However, we have estimated in comparison to the available direct EBL estimates that the eIGL should match the EBL to within 0%–35% in UV–optical–near-IR bandpasses and 0%–20% in far-IR bandpasses. These numbers are also consistent with the discrepancy between our eIGL measurements and the indirect VHE measurements. Specifically in the *J* band we find an eIGL value of 10.38 ± 1.52 while the H.E.S.S. Collaboration find a range for the EBL of 18.5–11.5 and the MAGIC team a range of 14.8–9.8. Formally our values are consistent. Again, this means that our value is low by 45% and 18% but with no ($<1\sigma$) significance. The important inference more that the eIGL and VHE EBL data show promising consistency, and if the errors in both can be reduced in significance then comparisons could potentially provide very interesting constraints on the diffuse universe.

3.7. The Integrated Energy of the COB and CIB

Finally, to determine the COB and CIB from our data we need to identify an appropriate fitting function. In this case the most straightforward option is to adopt a model that closely matches the data. Shown on Figures 4 and 5 is a model prediction from Andrews et al. (2016) that is based on an update to the two-component phenomenological model of Driver et al. (2013). In this model, we linked formation of spheroids to AGN activity, and adopted the axiom that formation of spheroids dominates at high redshift. The variation of AGN activity with redshift provides the shape, and the cosmic star formation history provides the normalization, for the star formation history of spheroids only. The star formation history of disks is then the discrepancy between the total cosmic star formation history and the star formation history of spheroids. With the star formation history of spheroids and disks defined, we use a code for stellar population synthesis and some underlying assumption of the evolution of metallicity (linear increase with star formation) to predict the cosmic spectral energy distribution at any epoch, and compare to the available data at $z < 0.1$ (see Driver et al.

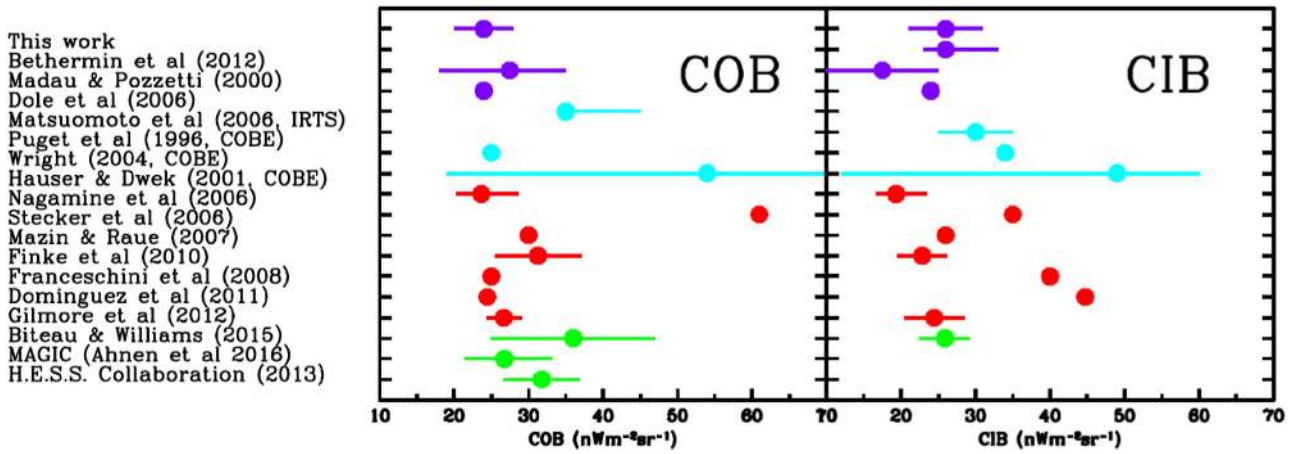

Figure 7. A selection of available COB and CIB measurements including eIGL estimates (mauve), direct measurements (cyan), numerical models (red), and VHE results (green). Error ranges are shown if provided.

2013 for full details). The model has now been developed to included obscured and unobscured AGNs, bolstering the UV flux, as well as dust reprocessing, and the model will be presented in detail in S. K. Andrews et al. (2016, in preparation).

In Figure 6 we again show our eIGL data compared to our adopted model, which provides a reasonable fit across the full wavelength range shown. We perform a standard error-weight χ^2-minimization of the model against the data to determine the optimal normalization and the 1σ error ranges on this normalization. Note that we fit the EBL data to the COB and CIB separately, and while the overall normalizations agree, the recovered 1σ errors are slightly broader for the CIB data (reflecting the large associated errors). We now integrate the EBL model using the R (INTEGRATE) function from 0.1 to 8 μm and 8 to 1000 μm to obtain the total energy contained within the COB and CIB. We find values of 24^{+4}_{-4} nW m^{-2} sr^{-1} and 26^{+5}_{-5} nW m^{-2} sr^{-1} respectively, essentially a 48%:52% split.

Figure 7 shows some of the COB and CIB measurements reported in the literature based on either integrated galaxy counts (mauve), direct estimates (cyan), numerical models (red), or VHE data (green). Our values agree well with previous eIGL estimates, and in particular with the most recent CIB measurement of Béthermin et al. (2012) (27^{+7}_{-3} nW m^{-2} sr^{-1}). This should not be particularly surprising because our CIB fits lean heavily on the source-count data of Béthermin, but the consistency in the measurement and errors is reassuring. In general we do see a trend—that the eIGL values are the lowest, the direct estimates the highest, and the VHE data are closer to, but slightly higher than, the eIGL estimates. This does imply that there may indeed be an additional diffuse component (photon field) at the ~20% level. As discussed above, this could plausibly be due to some combination of low-surface-brightness galaxies, intrahalo light, and/or any diffuse radiation from reionization. At the moment the errors are too broad to draw any firm conclusion; however, as observations improve in wide-area imaging (*Euclid, WFIRST, LSST*) and in VHE capabilities, there is a strong possibility of placing a meaningful constraint on this diffuse component. In our analysis the dominant errors in the COB, at least, are very much due to cosmic variance, and are currently at the 5%–10% level but can conceivably be reduced to below 1% in the near future. The normalized EBL model is available online in FITS format in a .tar.gz package.

4. SUMMARY

We have brought together a number of panchromatic data sets (GAMA, COSMOS/G10, *HST* ERS, UVUDF, and other mid- and far-IR data) to produce galaxy number-counts that typically span over 10 mag and extend from the far UV to the far IR. Having homogenized the data, we apply a consistent methodology to derive an IGL measurement and an extrapolated IGL (eIGL) measurement. The method avoids traditional models of galaxy number-counts; since all data sets are bounded in terms of the contribution to the IGL, they are simply fit with a 10-point spline. Integrating the spline with or without extrapolation then leads to a complete set of IGL measurements from the far UV to far IR. Our error analysis includes four key components: a systematic photometry and/or zero-point offset of $\pm$0.05 mag in all data sets, a refit based on 8- or 12-point splines, 10,001 Monte Carlo realizations of the random errors, and 10,001 Monte Carlo realizations of the estimates of cosmic variance. We combine the errors linearly to produce our final eIGL measurements, which are accurate to 2%–30% depending on bandpass.

In comparison to previous data we generally agree with previous IGL measurements, agree with direct measurements in the far IR, but disagree with direct measurements in the optical (see Figure 4, blue data points). We question whether the Milky Way or zodiacal light model requires revisiting for the direct optical and near-IR measurements. In particular we note (see Figure 6) that the direct estimates from *Pioneer* agree well with our eIGL estimates, as do the constraints from very high-energy experiments, suggesting a possible issue with the model of dust in the inner solar system.

We briefly acknowledge that the eIGL measurements could potentially miss light from low-surface-brightness systems (0%–20%) and intracluster/group light (0%–35%). Insofar as studies exist, evidence suggests that such emissions are likely small (<20%) and within our quoted errors. However, studies to further constrain both the space density of low-surface-brightness galaxies and the intrahalo light would clearly be pertinent.

Finally we overlay the two-component model of Driver et al. (2013), which now includes AGNs (S. K. Andrews et al. 2016,

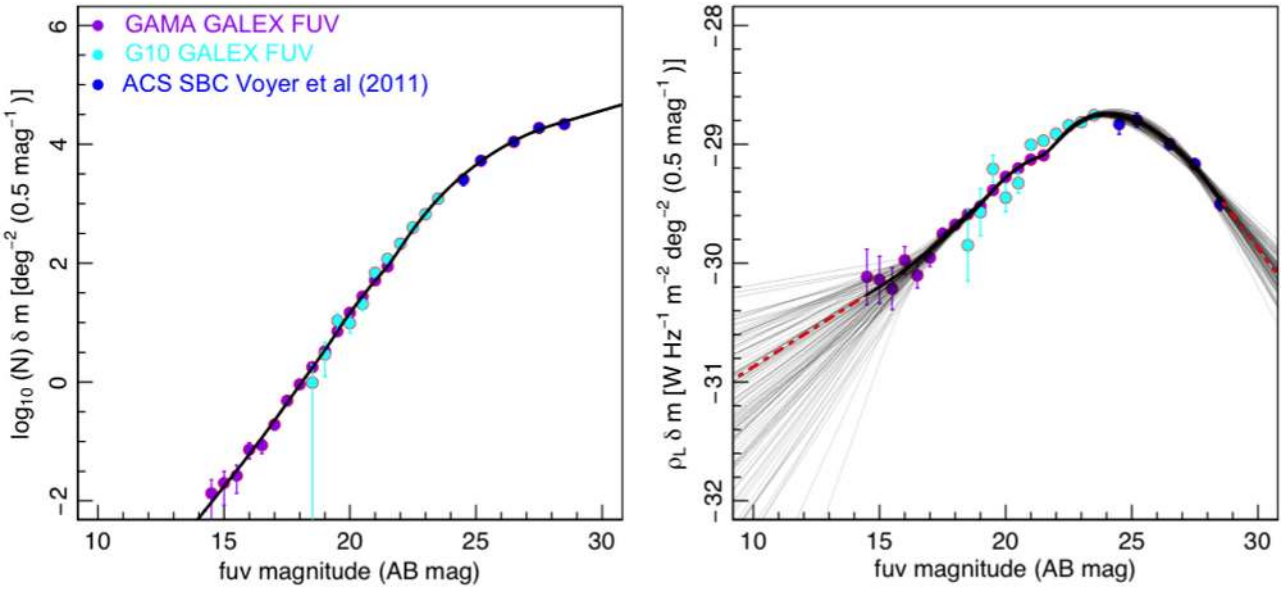

Figure 8. Left: galaxy number-counts in the FUV band, where the black curve depicts the 10-point spline fit to the luminosity density data. Right: the contribution of each magnitude interval to the luminosity density. Where the spline fit is extrapolated this is shown as a red dashed line. Also shown are 101 faint gray lines indicating identical fits to data randomly perturbed within their error bars. The other bands are shown in the Figure Set.

(The complete figure set (18 images) is available.)

in preparation), and find that we can explain the eIGL distribution rather trivially in terms of a phase of spheroid/AGN formation ($z > 1.5$), followed by disk formation ($z < 1.5$). Using a slightly modified version of the model as a fitting function we find that the COB and CIB contain 24^{+4}_{-4} nW m^{-2} sr^{-1} and 26^{+5}_{-5} nW m^{-2} sr^{-1} respectively, essentially a 48%:52% split.

We note that, over the coming years, with the advent of wide-field space-based imaging, and in particular *Euclid* and *WFIRST*, there will be great potential to constrain the UV, optical, and near-IR optical backgrounds to below 1%.

We thank the anonymous referee for comments that led to improvements in the paper, in particular the inclusion of cosmic variance errors.

We thank Adriano Fontana for providing the HUGS *K*-band number-count data. S.P.D. acknowledges support from the Australian Research Council via Discovery Project DP130103505. R.A.W. acknowledges support from NASA *James Webb Space Telescope* Interdisciplinary Scientist grant NAG5-12460 from GSFC. L.D. acknowledges support from the European Research Council in the form of Advanced investigator Grant, COSMICISM, and consolidated grant CosmicDust. S.K.A. and A.H.W. are supported by the Australian Government's Department of Industry Australian Postgraduate award.

GAMA is a joint European–Australasian project based around a spectroscopic campaign using the Anglo-Australian Telescope. The GAMA input catalog is based on data taken from the Sloan Digital Sky Survey and the UKIRT Infrared Deep Sky Survey. Complementary imaging of the GAMA regions is being obtained by a number of independent survey programmes including *GALEX* MIS, VST KiDS, VISTA VIKING, *WISE*, *Herschel*-ATLAS, GMRT, and ASKAP, providing UV to radio coverage. GAMA is funded by the STFC (UK), the ARC (Australia), the AAO, and the participating institutions. The GAMA website is http://www.gama-survey.org/. Based on observations made with ESO Telescopes at the La Silla Paranal Observatory under programme ID 179.A-2004.

The COSMOS/G10 data are based on the spectroscopic catalog of Davies et al. (2015), containing a reanalysis of the zCOSMOS data (Lilly et al. 2007) obtained from observations made with ESO Telescopes at the La Silla or Paranal Observatories under programme ID 175.A-0839. Photometric measurements are outlined in Andrews et al. (2016) and use data acquired as part of the Cosmic Evolution Survey (COSMOS) project, derived using the LAMBDAR software (Wright et al. 2016). All data and derived products are available via the COSMOS/G10 web portal: http://ict.icrar.org/cutout/G10/. This web portal is hosted and maintained by funding from the International Centre for Radio Astronomy Research (ICRAR) at the University of Western Australia.

Data from a wide-range of facilities are included in this paper and we wish to acknowledge the hard work and efforts of those involved in the design, construction, operation, and maintenance of these facilities, along with the science teams for having made their data sets readily available: *GALEX, Hubble Space Telescope, Herschel Space Observatory, Spitzer,* SDSS, *CFHT,* Subaru, Large Binocular Telescope, *WISE,* ESO *(HAWK-I on UT4)*, the Visible and Infrared Survey Telescope for Astronomy, H.E.S.S. and MAGIC.

APPENDIX
ADDITIONAL WAVEBANDS

Figure Set 8 shows the figures of number-counts and luminosity density for those data sets not shown in Figure 2, i.e., FUV/NUV, ugi, *ZYJHK*, *IRAC*-2 and 4, MIPS24, PACS70/100/160, and SPIRE 350/500. The description of the lines, labels, and key is as for Figure 2.

REFERENCES

Aharonian, F., Akhperjanian, A. G., Bazer-Bachi, A. R., et al. 2006, Natur, 440, 1018
Ahnen, M. L., Ansoldi, S., Antonelli, L. A., et al. 2016, A&A, 590, 24
Alexander, D. M., Bauer, F. E., Chapman, S. C., et al. 2005, ApJ, 632, 736
Andrews, S. K., Driver, S. P., Davies, L. J., et al. 2016, MNRAS, submitted
Ashby, M. L. N., Willner, S. P., Fazio, G. G., et al. 2015, ApJS, 218, 33
Barmby, P., Huang, J.-S., Ashby, M. L. N., et al. 2008, ApJS, 177, 431
Bernstein, G. M., Nichol, R. C., Tyson, J. A., Ulmer, M. P., & Wittman, D. 1995, AJ, 110, 1507
Bernstein, R. A. 2007, ApJ, 666, 663
Bernstein, R. A., Freedman, W. L., & Madore, B. F. 2002, ApJ, 571, 56
Berta, S., Magnelli, B., Nordon, R., et al. 2011, A&A, 532, A49
Bertin, E., & Arnouts, S. 1996, A&AS, 117, 393
Béthermin, M., Dole, H., Beelen, A., & Aussel, H. 2010, A&A, 512, A78
Béthermin, M., Le Floc'h, E., Ilbert, O., et al. 2012, A&A, 542, A58
Biteau, J., & Williams, D. A. 2015, ApJ, 812, 60
Cambrésy, L., Reach, W. T., Beichman, C. A., & Jarrett, T. H. 2001, ApJ, 555, 563
Capak, P., Aussel, H., Ajiki, M., et al. 2007, ApJS, 172, 99
Cluver, M. E., Jarrett, T. H., Hopkins, A. M., et al. 2014, ApJ, 782, 90
Cooray, A., Gong, Y., Smidt, J., & Santos, M. G. 2012, ApJ, 756, 92
Davies, J. I., Davies, L. J. M., & Keenan, O. C. 2016, MNRAS, 456, 1607
Davies, L. J. M., Driver, S. P., Robotham, A. S. G., et al. 2015, MNRAS, 447, 1014
de Oliveira-Costa, A., Tegmark, M., Gaensler, B. M., et al. 2008, MNRAS, 388, 247
Dole, H., Lagache, G., Puget, J.-L., et al. 2006, A&A, 451, 417
Domínguez, A., Primack, J. R., Rosario, D. J., et al. 2011, MNRAS, 410, 2556
Driver, S. P. 1999, ApJL, 526, L69
Driver, S. P., Hill, D. T., Kelvin, L. S., et al. 2011, MNRAS, 413, 971
Driver, S. P., Liske, J., Cross, N. J. G., De Propris, R., & Allen, P. D. 2005, MNRAS, 360, 81
Driver, S. P., Popescu, C. C., Tuffs, R. J., et al. 2008, ApJL, 678, L101
Driver, S. P., & Robotham, A. S. G. 2010, MNRAS, 407, 2131
Driver, S. P., Robotham, A. S. G., Bland-Hawthorn, J., et al. 2013, MNRAS, 430, 2622
Driver, S. P., Wright, A. H., Andrews, S. K., et al. 2016, MNRAS, 455, 3911
Dunne, L., Gomez, H. L., da Cunha, E., et al. 2011, MNRAS, 417, 1510
Dwek, E., & Arendt, R. G. 1998, ApJL, 508, L9
Dwek, E., Arendt, R. G., Hauser, M. G., et al. 1998, ApJ, 508, 106
Dwek, E., & Krennrich, F. 2013, APh, 43, 112
Eales, S., Dunne, L., Clements, D., et al. 2010, PASP, 122, 499
Eke, V. R., Baugh, C. M., Cole, S., et al. 2005, MNRAS, 362, 1233
Finke, J. D., Razzaque, S., & Dermer, C. D. 2010, ApJ, 712, 238
Fixsen, D. J., Dwek, E., Mather, J. C., Bennett, C. L., & Shafer, R. A. 1998, ApJ, 508, 123
Fontana, A., Dunlop, J. S., Paris, D., et al. 2014, A&A, 570, A11
Franceschini, A., Rodighiero, G., & Vaccari, M. 2008, A&A, 487, 837
Frayer, D. T., Sanders, D. B., Surace, J. A., et al. 2009, AJ, 138, 1261
Gardner, J. P., Brown, T. M., & Ferguson, H. C. 2000, ApJL, 542, L79
Gilmore, R. C., Somerville, R. S., Primack, J. R., & Domínguez, A. 2012, MNRAS, 422, 3189
Grazian, A., Menci, N., Giallongo, E., et al. 2009, A&A, 505, 1041
Hammer, D., Verdoes Kleijn, G., Hoyos, C., et al. 2010, ApJS, 191, 143
Hauser, M. G., Arendt, R. G., Kelsall, T., et al. 1998, ApJ, 508, 25
Hauser, M. G., & Dwek, E. 2001, ARA&A, 39, 249
H.E.S.S. Collaboration, Abramowski, A., Acero, F., et al. 2013, A&A, 550, A4
Hill, D. T., Kelvin, L. S., Driver, S. P., et al. 2011, MNRAS, 412, 765
Hopkins, A. M., Driver, S. P., Brough, S., et al. 2013, MNRAS, 430, 2047
Hopwood, R., Serjeant, S., Negrello, M., et al. 2010, ApJL, 716, L45
Inoue, Y., Inoue, S., Kobayashi, M. A. R., et al. 2013, ApJ, 768, 197
Jarrett, T. H., Cohen, M., Masci, F., et al. 2011, ApJ, 735, 112
Jauzac, M., Dole, H., Le Floc'h, E., et al. 2011, A&A, 525, A52
Kashlinsky, A. 2006, NewAR, 50, 208
Keenan, R. C., Barger, A. J., Cowie, L. L., & Wang, W.-H. 2010, ApJ, 723, 40
Khaire, V., & Srianand, R. 2015, ApJ, 805, 33
Koda, J., Yagi, M., Yamanoi, H., & Komiyama, Y. 2015, ApJL, 807, L2
Krick, J. E., Surace, J. A., Thompson, D., et al. 2009, ApJS, 185, 85
Lagache, G., Abergel, A., Boulanger, F., Désert, F. X., & Puget, J.-L. 1999, A&A, 344, 322
Lagache, G., Puget, J.-L., & Dole, H. 2005, ARA&A, 43, 727
Levenson, L., Marsden, G., Zemcov, M., et al. 2010, MNRAS, 409, 83
Levenson, L. R., & Wright, E. L. 2008, ApJ, 683, 585
Lilly, S. J., Le Fèvre, O., Renzini, A., et al. 2007, ApJS, 172, 70
Liske, J., Baldry, I. K., Driver, S. P., et al. 2015, MNRAS, 452, 2087
Liske, J., Lemon, D. J., Driver, S. P., Cross, N. J. G., & Couch, W. J. 2003, MNRAS, 344, 307
Lutz, D., Poglitsch, A., Altieri, B., et al. 2011, A&A, 532, A90
Madau, P., & Pozzetti, L. 2000, MNRAS, 312, L9
Madau, P., & Silk, J. 2005, MNRAS, 359, L37
Magnelli, B., Popesso, P., Berta, S., et al. 2013, A&A, 553, A132
Matsumoto, T., Kim, M. G., Pyo, J., & Tsumura, K. 2015, ApJ, 807, 57
Matsumoto, T., Matsuura, S., Murakami, H., et al. 2005, ApJ, 626, 31
Matsumoto, T., Seo, H. J., Jeong, W.-S., et al. 2011, ApJ, 742, 124
Matsuoka, Y., Ienaka, N., Kawara, K., & Oyabu, S. 2011, ApJ, 736, 119
Mattila, K. 2006, MNRAS, 372, 1253
Mazin, D., & Raue, M. 2007, A&A, 471, 439
McCracken, H. J., Milvang-Jensen, B., Dunlop, J., et al. 2012, A&A, 544, A156
McVittie, G. C., & Wyatt, S. P. 1959, ApJ, 130, 1
Mihos, J. C., Harding, P., Feldmeier, J., & Morrison, H. 2005, ApJL, 631 L41
Montes, M., & Trujillo, I. 2014, ApJ, 794, 137
Nagamine, K., Ostriker, J. P., Fukugita, M., & Cen, R. 2006, ApJ, 653, 881
Oliver, S. J., Bock, J., Altieri, B., et al. 2012, MNRAS, 424, 1614
Papovich, C., Dole, H., Egami, E., et al. 2004, ApJS, 154, 70
Partridge, R. B., & Peebles, P. J. E. 1967a, ApJ, 148, 377
Partridge, R. B., & Peebles, P. J. E. 1967b, ApJ, 147, 868
Presotto, V., Girardi, M., Nonino, M., et al. 2014, A&A, 565, A126
Puget, J.-L., Abergel, A., Bernard, J.-P., et al. 1996, A&A, 308, L5
R Core Team. 2015, https://www.R-project.org/
Rafelski, M., Teplitz, H. I., Gardner, J. P., et al. 2015, AJ, 150, 31
Rudick, C. S., Mihos, J. C., & McBride, C. K. 2011, ApJ, 732, 48
Sanders, D. B., Salvato, M., Aussel, H., et al. 2007, ApJS, 172, 86
Scoville, N., Aussel, H., Brusa, M., et al. 2007, ApJS, 172, 1
Shanks, T., Georgantopoulos, I., Stewart, G. C., et al. 1991, Natur, 353, 315
Smith, A. J., Wang, L., Oliver, S. J., et al. 2012, MNRAS, 419, 377
Somerville, R. S., Gilmore, R. C., Primack, J. R., & Domínguez, A. 2012, MNRAS, 423, 1992
Stecker, F. W., Malkan, M. A., & Scully, S. T. 2006, ApJ, 648, 774
Taniguchi, Y., Scoville, N., Murayama, T., et al. 2007, ApJS, 172, 9
Teplitz, H. I., Rafelski, M., Kurczynski, P., et al. 2013, AJ, 146, 159
Totani, T., Yoshii, Y., Iwamuro, F., Maihara, T., & Motohara, K. 2001, ApJL, 550, L137
Valiante, E., Smith, M. W. L., Eales, S., et al. 2016, MNRAS, submitted (arXiv:1606.09615)
van Dokkum, P. G., Abraham, R., Merritt, A., et al. 2015, ApJL, 798, L45
Viero, M. P., Wang, L., Zemcov, M., et al. 2013, ApJ, 772, 77
Voyer, E. N., Gardner, J. P., Teplitz, H. I., Siana, B. D., & de Mello, D. F. 2011, ApJ, 736, 80
Wang, L., Viero, M., Clarke, C., et al. 2014, MNRAS, 444, 2870
Wardlow, J. L., Cooray, A., De Bernardis, F., et al. 2013, ApJ, 762, 59
Watkins, A. E., Mihos, J. C., Harding, P., & Feldmeier, J. J. 2014, ApJ, 791, 38
Wesson, P. S. 1991, ApJ, 367, 399
Wesson, P. S., Valle, K., & Stabell, R. 1987, ApJ, 317, 601
Windhorst, R. A., Cohen, S. H., Hathi, N. P., et al. 2011, ApJS, 193, 27
Wright, A., Robotham, A. S. G., Bourne, N., et al. 2016, MNRAS, 460, 765
Wright, E. L. 2004, NewAR, 48, 465
Xu, C. K., Donas, J., Arnouts, S., et al. 2005, ApJL, 619, L11
Zamojski, M. A., Schiminovich, D., Rich, R. M., et al. 2007, ApJS, 172, 468
Zemcov, M., Smidt, J., Arai, T., et al. 2014, Sci, 346, 732
Zwicky, F. 1951, PASP, 63, 61